Supporting Information for

¹³C ENDOR Spectroscopy of Lipoxygenase-Substrate Complexes Reveals the Structural Basis for C-H Activation by Tunneling

Masaki Horitani,[1^] Adam R. Offenbacher,[2^] Cody A. Marcus Carr,[2‡] Tao Yu,[3] Veronika Hoeke,[1] George E. Cutsail III,[1,3] Sharon Hammes-Schiffer,[4] Judith P. Klinman,[2,5*] and Brian M. Hoffman[1*]

[1]Department of Chemistry, Northwestern University, Evanston, Illinois 60208, United States

[2]Department of Chemistry and California Institute for Quantitative Biosciences (QB3), University of California, Berkeley, California 94720, United States

[3]Max Planck Institute for Chemical Energy Conversion, Stiftstr. 34−36, D-45470 Mülheim an der Ruhr, Germany

[4]Department of Chemistry, University of Illinois at Urbana-Champaign, Urbana, Illinois 61801, United States

[5]Department of Molecular and Cell Biology, University of California, Berkeley, California 94720, United States

[^]Contributed equally

[‡]Current Address: Riffyn, Oakland, California 94612, United States

* Corresponding Authors; email: bmh@northwestern.edu (B.M.H.); klinman@berkeley.edu (J.P.K)

Extended Results and Discussion:

EPR/ENDOR Simulations.

   As mentioned in the text, EPR and ENDOR simulations involved a Gaussian distribution in the ZFS parameters, D and λ (= E/D). In EPR simulations, the EasySpin 5.0 program allows to account for spectral broadenings originating from ZFS distributions by incorporating 'DStrain', which specifies Gaussian distributions of the scalar parameters D and E. However, this routine is not adequate for the breadth of distributions in SLO, and in any case, in ENDOR simulations the EasySpin routine does not take into account DStrain or any other type of distribution in ZFS parameters. To employ the same ZFS distributions in EPR and ENDOR simulations (i.e. determine best values from EPR and subsequently use them in ENDOR simulations), we have avoided the use of DStrain, and instead as suggested on the EasySpin home page, manually incorporated a Gaussian distribution in D and E in both the EPR and the ENDOR simulations, as seen below in the MATLAB script for EPR simulations. Our script runs a loop over a selected number of equally spaced D (E) values around a mean D_0 (E_0) value, and sums up the associated spectra properly weighted according to the Gaussian distribution function. The script presented incorporates a loop over D_0, E_0. A factor f is used to specify the width of the Gaussian distribution as a fraction of its mean value, assuming the same value of f for the distributions in the two ZFS parameters D and E.

Matlab Script

```
N_D_vector = linspace(5,7,2);
N_E_vector = linspace(3,9,3);
D0_vector = 1320 + linspace(-1,1,1)*0;
E0_over_D0_vector = 0.17 + linspace(-1,1,1)*0.00;
f_vector = 0.32 + linspace(-1,1,1)*0.00;


for i = 1:length(N_D_vector)
    N_D = N_D_vector(i); % number of points in D distribution
    stepvec_D = linspace(-1,1,N_D);
    for j = 1:length(N_E_vector)
        N_E = N_E_vector(j); % number of points in E distribution
        stepvec_E = linspace(-1,1,N_E);
        for k = 1:length(D0_vector)
            D0 = D0_vector(k);
            for l = 1:length(E0_over_D0_vector)
                E0_over_D0 = E0_over_D0_vector(l);
                E0 = E0_over_D0*D0;
                for m = 1:length(f_vector)
                    f = f_vector(m);
                    % D distribution
                    a = f*D0; % a = 1/2*FWHM
                    sigma_D = a/sqrt(2*log(2)); % computed for given a
                    D_range = D0 + stepvec_D*2*sigma_D; % vector of N points
from D0-2*sigma to D0+2*sigma (confidence interval 95%)
```

```
%                    if length(D_range)>1
%                         stepsize_D = D_range(2)-D_range(1);
%                    end
                 weight_D = 1/(sigma_D*sqrt(2*pi))*exp(-(D_range-
D0).^2/(2*sigma_D^2)); % normal distribution of D
%                    % Integrals (for control)
%                    fun_D = @(D_range_int) 1/(sigma_D*sqrt(2*pi))*exp(-
(D_range_int-D0).^2/(2*sigma_D^2));
%                    int_D =
integral(fun_D,D_range(1),D_range(length(D_range))); % confidence level
%                    int_D_norm = integral(fun_D,-Inf,+Inf); % normalization
control

                 % E distribution
                 b = f*E0; % b = 1/2*FWHM
                 sigma_E = b/sqrt(2*log(2)); % computed for given b
                 E_range = E0 + stepvec_E*2*sigma_E; % vector of N points
from E0-2*sigma to E0+2*sigma (confidence interval 95%)
%                    if length(E_range)>1
%                         stepsize_E = E_range(2)-E_range(1);
%                    end
                 weight_E = 1/(sigma_E*sqrt(2*pi))*exp(-(E_range-
E0).^2/(2*sigma_E^2)); % normal distribution of E
%                    % Integrals (for control)
%                    fun_E = @(E_range_int) 1/(sigma_E*sqrt(2*pi))*exp(-
(E_range_int-E0).^2/(2*sigma_E^2));
%                    int_E =
integral(fun_E,E_range(1),E_range(length(E_range)));  % confidence level
%                    int_E_norm = integral(fun_E,-Inf,+Inf); % normalization
control

                 % Simulation
                 totalspc = 0;
                 for iw = 1:N_D
                     for kw = 1:N_E
                         Sys.D = [D_range(iw) E_range(kw)];
                         [B,sim_spec0] = pepper(Sys,Exp);
                         totalspc = totalspc +
weight_D(iw)*weight_E(kw)*sim_spec0;
                     end
                 end
             end
         end
     end
 end
end
```

Determination of ρ_{eff}.

When inferring Mn-^{13}C distances of non-coordinated ^{13}C nuclei from the electron-nuclear dipolar interaction parameter T, one needs to take into account that the $S = 5/2$ Mn^{2+} spin is partially delocalized over the ligands. To examine the influence of such spin delocalization, the dipolar interaction between the Mn^{2+} spin delocalized over the ligands of its coordination sphere

S3

and a ^{13}C nucleus at an arbitrary position was calculated as a sum of the dipolar interactions with the individual spin densities on Mn^{2+} and its six ligands (**eq S1**). The spin densities on the coordinated ligands of both Mn^{2+}-SLO and Mn^{2+}(H$_2$O)$_6$ have been calculated by QM-MM for the Mn-SLO and DFT methods for Mn^{2+}(H$_2$O)$_6$ (we acknowledge Prof. Martin Kirk for the latter computation). Using Mulliken or Loewdin spin population analysis gives spin densities in the range of 0.96-0.97 for Mn^{2+} in both calculations, and thus ~0.005 per ligand. This is in good agreement with earlier neutron diffraction studies indicating a spin density of 0.007 per H$_2$O of Mn^{2+}(H$_2$O)$_6$.[1]

The model calculation placed the ligand spins at the nominal Mn-Ligand distance of 2.18 Å derived from a Mn^{2+}(H$_2$O)$_6$ EXAFS study,[2] and used this value to calculate the dipolar sum,

$$\mathbf{T} = \sum_{i=1}^{7} \mathbf{T}_i \; ; \qquad \mathbf{T}_i = t_i \mathbf{M}_i \; ; \qquad t_i = \rho_i \left(\frac{2g\beta g_n \beta_n}{r_i^3} \right) ; \qquad (\text{S1})$$

where $\mathbf{M}_i$ is a 3×3 matrix that specifies the orientation of the X-^{13}C (X = Mn, Ligand) vector relative to the molecular frame. The weighting factors t_i are calculated based on the DFT-computed spin densities ρ_i on Mn^{2+} and its six ligands, and the corresponding X-^{13}C distances r_i. Diagonalization of the matrix sum, $\mathbf{T}$, yields the predicted principal values for the observed anisotropic coupling tensor,

$$\mathbf{T} = [T_1, T_2, T_3] \qquad (\text{S2})$$

plus orientation of that tensor relative to the molecular frame.

For hexa-coordinate Mn^{2+} with such a spin distribution, at Mn-^{13}C distances, $r \gtrsim 4$ Å, the sum in **eq S1** gives a net dipolar interaction precisely of the form $\mathbf{T} = [-T, -T, 2T]$. For the even longer Mn-^{13}C distances observed for SLO, the value of the sum precisely matches the point-dipole parameter, T, of **eq 2** by assigning an effective spin density, ρ_{eff}, = 0.994 to Mn. We have adopted this value to obtain ENDOR-derived Mn-^{13}C distances in Mn-SLO through use of **eq 2**.

Orientation Selection and Determination of A.

As shown in **Fig 3**, thermal depopulation of higher-lying m_s levels at 2 K leaves the S = 5/2 (Mn^{2+}) EPR spectrum with 'wings' that are exclusively associated with the m_s = -5/2 sublevel, with the field along the 'y' ZFS axis at the low-field edge of the EPR spectrum and the 'z' ZFS axis at the high-field edge and it selectively suppresses high-level manifolds. This enhanced orientation selectivity enables a determination of the hyperfine tensor of a ^{13}C label in LA, A, through simulation of the full 2D field-frequency pattern of multiple ENDOR spectra collected across the entire EPR envelope, as exemplified by **Fig 4**, with analysis yielding both principal values of A and its orientation relative to the ZFS coordinate frame for Mn^{2+} ion.[3-5] The simulations involved the EPR envelope whose description is discussed immediately above.

To begin the analysis, we examine the behavior of the high- and low-frequency edges of the spectra as the field of observation traverses the EPR envelope. As illustrated in **Fig S4**, inspection of these two spectra plus a spectrum collected at $g \sim 2$, gives a preliminary indication of the orientation of the Mn-^{13}C/^{1}H vectors with respect to the ZFS axes, and the value for T. Simulation of the full 2D pattern, as informed by such inputs, **Figs 4, S5 and S6** then yields the full hyperfine tensor, giving both accurate principal values and precise orientation relative to the ZFS tensor axes.

Error Analysis for Mn-^{13}C/^{1}H distances.

We here assess the precision and overall accuracy of the Mn-nuclear distances determined from the ENDOR measurements. We show that, even though the precision in

determining the orientations of the Mn-^{13}C vectors from the 2D ENDOR patterns is limited, $+/-x^0$ in θ, $+/-y^0$ in ϕ, one can obtain r to quite high experimental precision by focusing on the single-crystal-like spectra collected at the low-field edge, where the magnetic field is oriental along the y axis of the ZFS tensor, and only the $m_s = -5/2$ substate contributes,

In such a spectrum the magnitude of the hyperfine offset, denoted here as δv, of the $m_s = -5/2$ sublevel for a nucleus positioned at [r, θ, ϕ] within the ZFS coordinate frame is given by the T_{yy} component of the dipolar interaction expressed in that frame, and this offset determines r:

$$\delta v = \frac{5}{2} T_{yy}(r,\theta,\phi,\rho) = \frac{5}{2} t(r,\rho)[3\sin^2\theta\sin^2\phi - 1] \qquad t(r,\rho) = \frac{g\beta g_N \beta_N \rho}{r^3} \qquad (S3)$$

$$r = \left(\frac{5}{2} \frac{g\beta g_N \beta_N \rho}{\delta v}[3\sin^2\theta\sin^2\phi - 1] \right)^{1/3} \qquad (S4)$$

To assess the uncertainty in the experimentally derived value of r for the Mn-N vector, δr, we consider the differential dr with respect to the experimental parameters that determine it,

$$dr_y = \sum_{\delta v, \theta, \phi} \frac{\partial r}{\partial x_i} dx_i \qquad (S5)$$

then take the derivatives and rewrite as a relationship between experimental uncertainties,

$$\frac{\delta r}{r} = \frac{1}{3}\left[-\frac{\delta(\delta v)}{\delta v} + [3\sin^2\theta\sin^2\phi - 1]^{-1}\left([\sin 2\theta\sin^2\phi]\delta\theta - 3[\sin^2\theta\sin 2\phi]\delta\phi\right)\right] \qquad (S6)$$

$$dT_2 = \frac{\partial T_2}{\partial r}dr + \frac{\partial T_2}{\partial \theta}d\theta + \frac{\partial T_2}{\partial \theta}d\theta \ . \quad (S7)$$

This equation shows that the uncertainties are minimized by the experimental result that for ^{13}C11, ^{13}C10, and the ^{1}HOH nuclei, all lie very nearly in the x, z plane, namely are characterized by $\phi \rightarrow 0$. As each of the angle-dependent terms has a dependence on $\sin\phi$, and thus vanish as $\phi \rightarrow 0$, then $\delta r/r$ resulting from experimental error is simply,

$$\frac{\delta r}{r} \xrightarrow{\phi \rightarrow 0} \pm\frac{1}{3}\frac{\delta\delta v}{\delta v} \qquad (S8)$$

Examination of **Fig 5** indicates that the high resolution of the ENDOR spectra leads to a very small uncertainty in the ENDOR offset and low fractional uncertainty in the offset $\delta\delta v/\delta v \sim \pm 0.02$, with a one-third smaller experimental uncertainty in r:

$$\frac{\delta r}{r} \xrightarrow{\phi \rightarrow 0} \sim \pm 0.01 \qquad (S9)$$

There is, in principle, an additional uncertainty in determining r from the semi-empirical dipolar formula of **eq S3**. Variations in the choice of the effective spin density on Mn, ρ_{eff}, which adds an uncertainty r proportional to the uncertainty in ρ_{eff}.

$$\frac{\delta r}{r} \approx \pm \frac{1}{3} \frac{\delta \rho_{eff}}{\rho_{eff}} \quad \text{(S10)}$$

However, given the result that $\rho_{eff} \rightarrow 1$ (see above), this contribution is negligible.

Mutation-induced changes in linewidth assigned to changes in the distribution in r.

The linewidth of the ENDOR signals for the ^{13}C is the sum of the intrinsic contributions plus some contribution from a distribution in distances, δr, which leads to a distribution in ENDOR offsets. These two contributions cannot be determined individually, but we can assign a change in linewidth, δW, caused by mutation to a change in the distribution of distances, δr. By analogous procedures to those above we obtain the following relationship for the features in the low-field, single-crystal-like Mn-SLO/LA(^{13}C) ENDOR spectra:

$$\frac{\delta r}{r} \approx \frac{1}{3} \frac{\delta W}{\delta v} \quad \text{(S11)}$$

It is perhaps useful to note that the physical significance of the distribution breadth parameters, δr, as calculated from **eq S6** depends on the nature of the distribution. The calculated δr would apply directly to a distribution in which the substrates were disordered only along the Mn-C$_{in}$ vector, but otherwise these values represent a projection of the breadth of the disorder distribution onto that vector. As illustration, it can be shown that if C$_{in}$ were spherically distributed around a point at distance r from Mn, with a Gaussian distribution having a width parameter, δr^{sph}, then the apparent δr calculated from **eq S6** would be ~ 20% less than δr^{sph}: $\delta r/\delta r^{sph} = \sqrt{(2/3)}$.

The Orientation of Bound Water.

Fig S5 presents 2D field-frequency ^{1}H Davis ENDOR spectra for Mn-SLO/LA WT in H$_2$O and D$_2$O and their difference spectra. The difference spectra show only exchangeable protons, so the peaks of ligand water remain in the spectra and those of protons in His which is directly coordinated with Mn^{2+} ion are cancelled out. The lowest peak at 11,000 G, which is from m_s = -5/2 and -3/2 sublevels, has clearly doublet, denoted in **Fig S5**. This suggests that the ligand bound to Mn^{2+} ion is a water, or less likely from OH$^-$ two conformers. Same as ^{13}C analysis, this overall 2D pattern give us the information of the axis relative to zero field splitting. The set of angles for ^{1}H$_a$ with best fitting were $\phi = 0°$ (±5) and $\theta = 70°$ (±5). Importantly, this concluded that the direction from metal to water proton is almost along to the direction from metal to target carbons in LA ($\phi \sim 0°$).

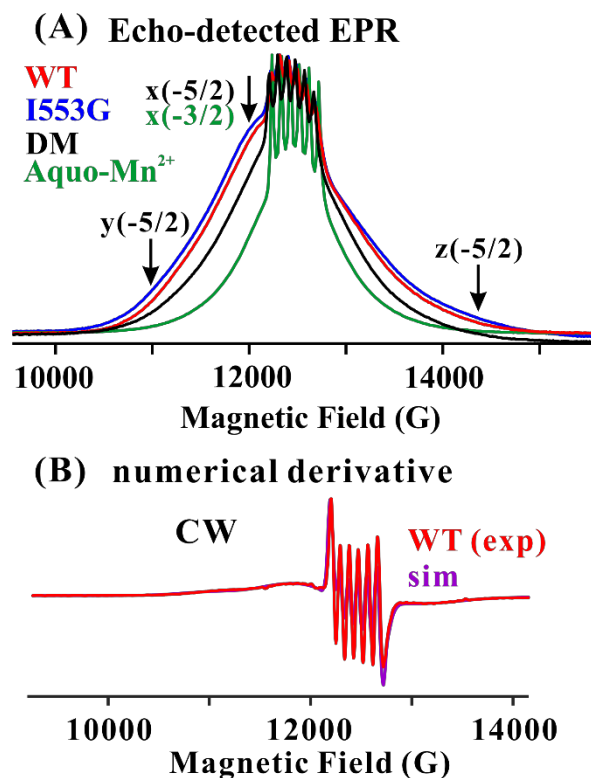**(A) Echo-detected EPR**

WT
I553G
DM
Aquo-Mn^{2+}

x(-5/2)
x(-3/2)

y(-5/2)

z(-5/2)

10000   12000   14000
Magnetic Field (G)

(B) numerical derivative

CW

WT (exp)
sim

10000   12000   14000
Magnetic Field (G)

Fig S1. (**A**) 35 GHz Hahn echo-detected EPR spectra of Mn-SLO with LA (WT; red, I553G; blue, DM; black) and [Mn^{2+}(H$_2$O)$_6$] compound (green). (**B**) The numerical derivative spectrum of 35 GHz CW EPR for Mn-SLO WT with LA (red) and simulation (purple). (**A**) Experimental conditions are; microwave frequency = 34.76 GHz, MW pulse length ($\pi/2$) = 40 ns, τ = 600 ns, reptition rate = 10 Hz and T = 2 K. (**B**) Experimental conditions and simulation parameters are same as **Fig 2A**.
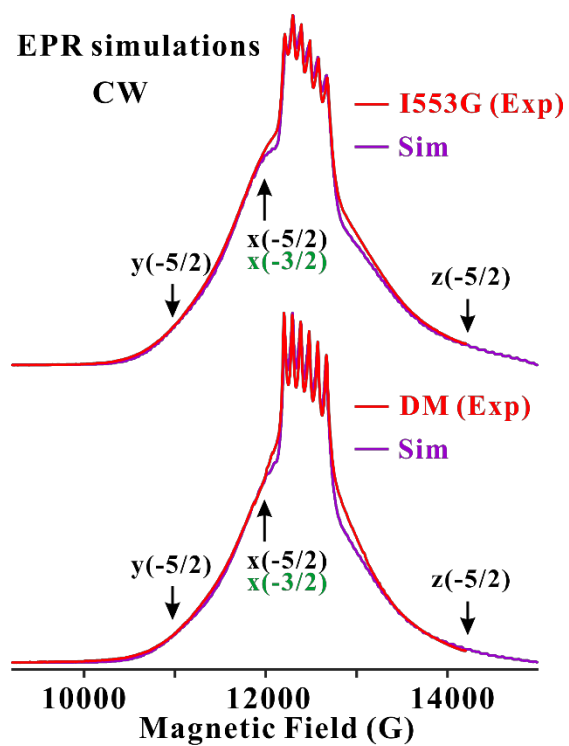
Fig S2. 35 GHz CW rapid-passage EPR spectra (red) and simulation (purple) for Mn-SLO I553G (upper) and DM (lower) with LA at 2 K. Conditions are same as **Fig 2A**. Simulation parameters are listed in **Table 1**.
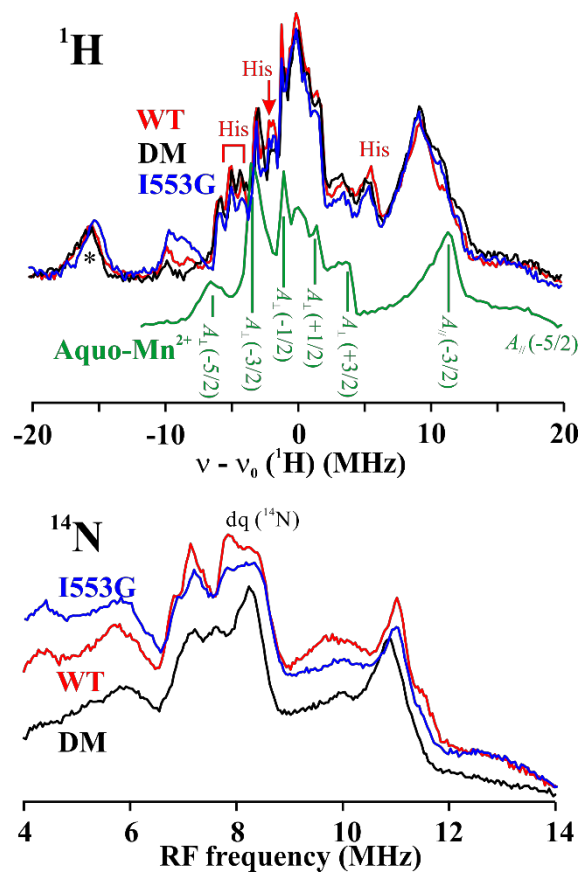
Fig S3. 35 GHz ^{1}H and ^{14}N Davies ENDOR spectra for WT Mn-SLO and mutants, plus aquo-Mn^{2+}. Spectra were collected at the center of well-resolved 6 line hyper-fine splitting of EPR spectrum in each sample. Assignments of ^{1}H ENDOR transitions taken from the work of Scholes and coworkers.[6] A tentative assignment of signals from histidine protons of Mn-SLO is included, as is an assignment (*) of a ^{55}Mn ENDOR harmonic.[7] An apparent sharpening of the double-quantum (dq) ^{14}N transitions is consistent with the elimination of a slight inequality in the ^{14}N hyperfine couplings of the three histidines. *Conditions:* microwave frequency = ~34.78 GHz, MW pulse length ($\pi/2$, π, $\pi/2$) = 120, 60, 120 ns, τ = 600 ns, repetition rate = 100 Hz and T = 2 K. The Larmor frequency of ^{14}N at this magnetic field is ~ 3.83 MHz.
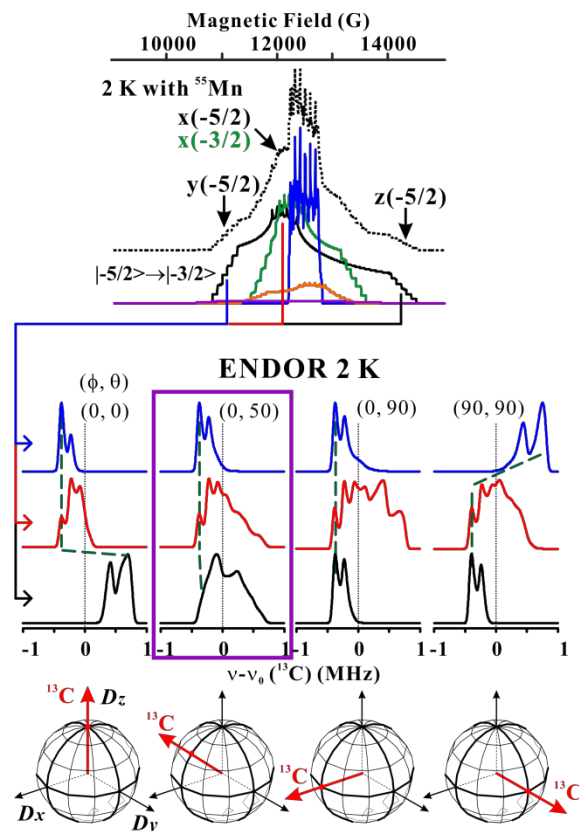
Fig S4. (**upper**) Idealized EPR simulation for D = +1250 MHz, λ = 0.20 at 2 K. (**middle**) 2D field-frequency patterns of 35 GHz ^{13}C (I = 1/2) ENDOR simulations for this S = 5/2 center with (**lower**) various orientations of the Mn-^{13}C vector relative to the ZFS. Red arrows in the unit spheres indicate the vector between Mn and the target ^{13}C; box is around an orientation that corresponds to $^{13}C10$ (WT). The green dashed lines in ENDOR simulations (middle) indicate the peak position of the m_s = -5/2 ENDOR spectrum. The magnetic fields of ENDOR simulation at the high (black, bottom) and low fields (blue, top) correspond to single-crystal like ENDOR responses from the m_s = -5/2, -3/2 substates with the external field along the y and z-axes of ZFS, respectively; intermediate field (red, middle) is from multipole substates, with the x-axis orientation dominant.
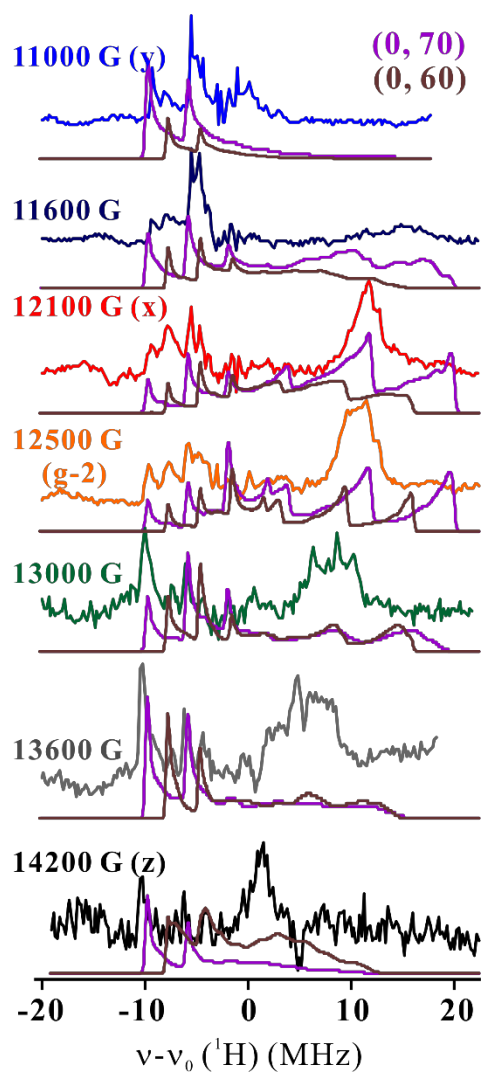
Fig S5. 2D field-frequency 35 GHz Davis ^{1}H ENDOR difference spectra for Mn-SLO WT in H_2O and D_2O with two distinct best fit simulation (purple and brown). The difference spectra were yielded by the subtraction the spectra in D_2O from ones in H_2O. Experimental conditions: microwave frequency = ~34.73 GHz, MW pulse length ($\pi/2$) = 60 ns, τ = 600 ns, repetition rate = 100 Hz and $T = 2$ K. Simulation parameters are listed in **Table 2**.
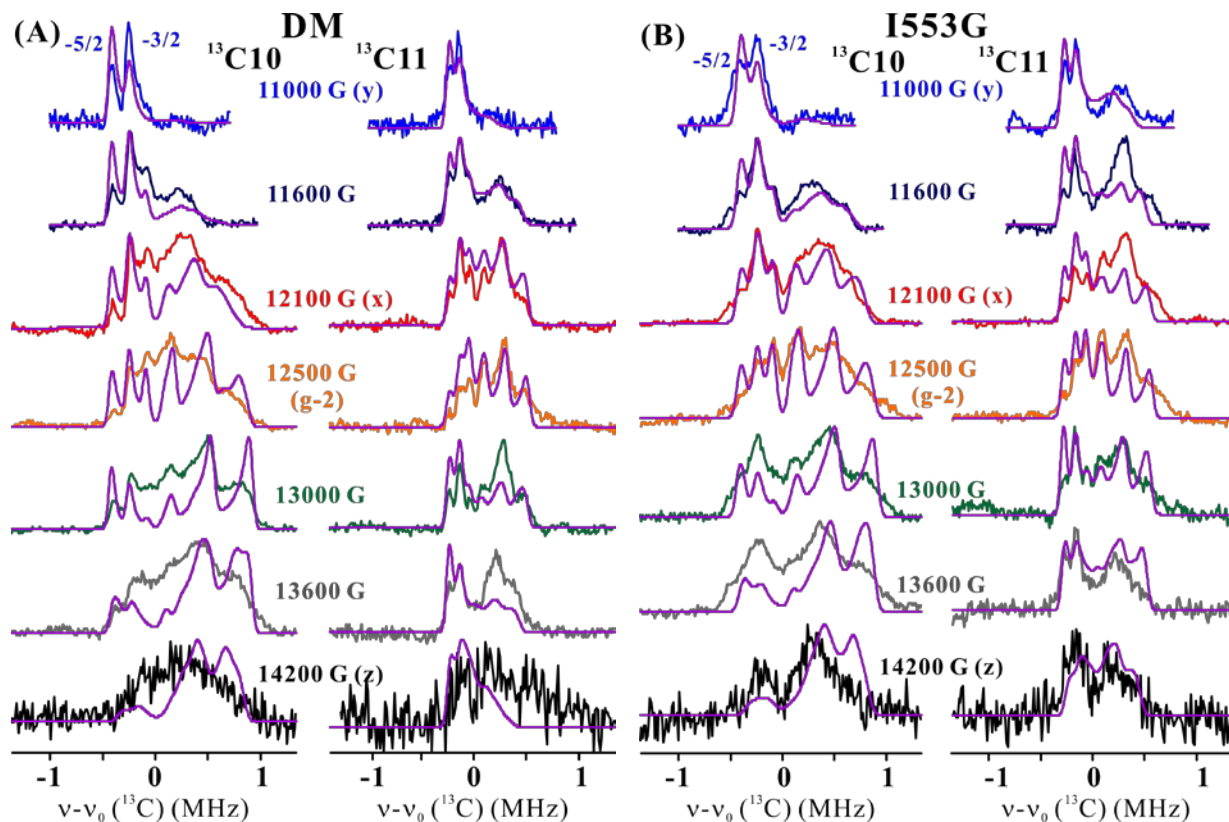
Fig S6. 35 GHz 2D field-frequency pattern ^{13}C Mims ENDOR for (**A**) DM and (**B**) I553G with ^{13}C10- and ^{13}C11-LA and simulation (purple) at 2 K. Simulation for WT ^{13}C11-LA of individual conformers, *a* and *b*, are shown in black and gray slashed lines, respectively. The ratio of populations, *a*/*b* ratio, is that same at all fields Conditions are same as **Fig 2**. Simulation parameters are listed in **Table 2**.
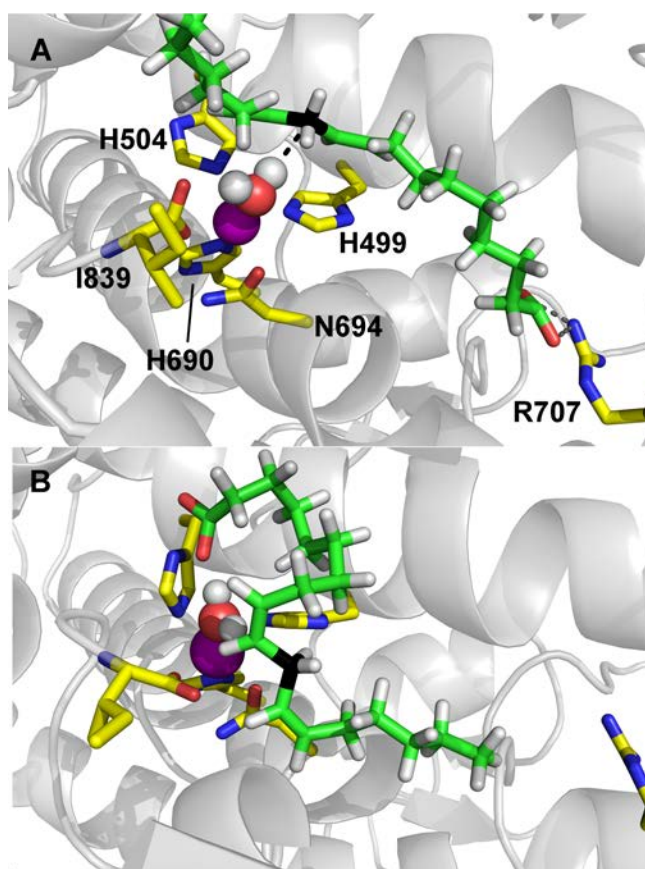
Fig S7. Final frames of the MD simulations for the two binding orientations of the LA for WT Mn-SLO. (**A**) shows the "carboxylate in" orientation, in which the carboxylate group of LA is hydrogen bonded to R707 of SLO. Residues comprising first ligand sphere of Mn are labeled for clarity. (**B**) shows the "carboxylate out" orientation. The color scheme is as follows: carbons are green for LA, black for C11, and yellow for relevant SLO side chains; oxygens are red; nitrogens are blue; hydrogens are white; manganese is purple.
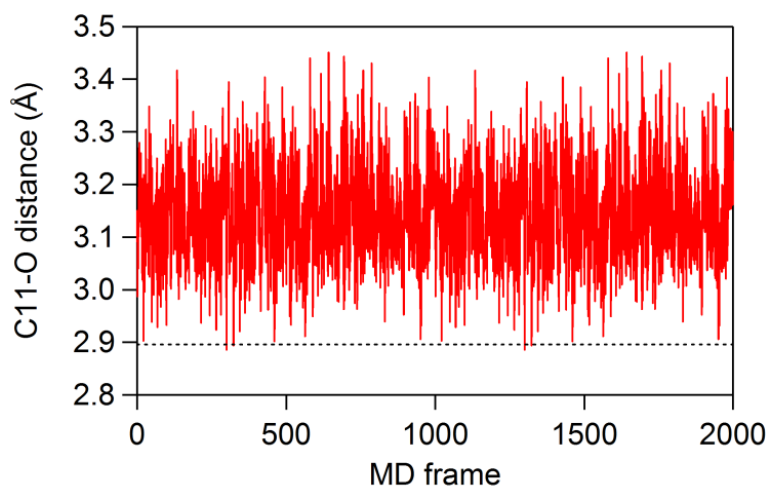
Fig S8. The C11-O distance (in Å) during the course of the two 50 ns MD trajectories for WT Mn-SLO system with LA in the "carboxylate in" orientation. Each frame represents 50 ps. The dashed line represents 2.9 Å, and only 4 out of 2000 frames show C11-O distances that are equal to or less than this distance.
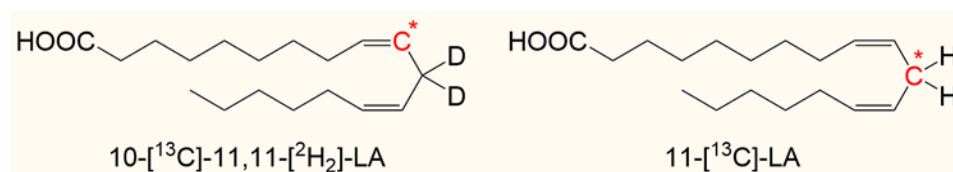
Fig S9. Structures and labeling schemes for the two ^{13}C (red asterisks) labeled linoleic acid substrates used in the ENDOR measurements. Note that 10-[^{13}C]-11,11-[^{2}H$_2$]-LA (denoted ^{13}C10 throughout the text) is dideuterated (shown as D) at the reactive carbon (C11). The deuterium incorporation at C11 for the ^{13}C10 substrate was designed for backbone kinetic isotope measurements in the ferric form of SLO as described in ref [8]. Deuterium labeling to slow down the reaction is not necessary for the ENDOR measurements because the Mn^{2+} form of SLO is unreactive and the samples are prepared anaerobically. In fact, we demonstrate that no turnover is observed for the natural abundance LA under these conditions (see **Methods** for details). For this reason, 11-[^{13}C]-LA, denoted as ^{13}C11 throughout the text) was not synthesized with deuterium at the reactive carbon.

Table S1. Kinetic parameters for Fe-SLO variants, compared to native Mn-containing lipoxygenase (MnLOX)[a]

	k_{cat} (s⁻¹)	E_a (kcal/mol)	$^{D}k_{cat}$	ΔE_a (kcal/mol)	Ref
Fe-SLO variants					
WT SLO	297 (12)	2.1 (0.2)	81 (5)	0.9 (0.2)	9
DM SLO	0.021 (0.001)	9.9 (0.2)	537 (55)[b]	N.D.[c]	10
I553G SLO	58 (4)	0.03 (0.04)	178 (16)	5.3 (0.7)	11
MnLOX from *G. graminis*					
MnLOX[d]	18-26	*ca.* 11	*ca.* 22	N.D.[c]	12,13

[a]Unless otherwise noted, kinetic parameters are listed for reactions in 0.1 M borate, pH 9.0 and k_{cat}, K_M and $^{D}k_{cat}$ values are reported for 30˚C. Standard deviations are shown in "( )".

[b]Determined by pre-steady-state kinetics at 35˚C. The steady state $^{D}k_{cat}$ = 729 (26) at 30˚C.

[c]N.D., Not determined.

[d]Native manganese-containing lipoxygenase from the take-all fungus, *G. graminis.* As isolated, contains 0.8 Mn per monomer. Reaction kinetics were determined by UV/vis absorption of HPOD production. The pH optimum is 7. The ratio of 13*R*-HPOD to 11*S*-HPOD is significantly pH dependent. Temperature for k_{cat}, K_M, and $^{D}k_{cat}$ is 25˚C. Errors/uncertainties were not reported; the kinetic values are only approximate.

Table S2. Metal-ligand distances in SLO vs fungal MnLOX from X-ray crystal structures

atom	SLO		MnLOX	
	Fe–X (Å)[a]	Mn–X (Å)[b]	Atom	Mn–X (Å)[c]
His499 Nε2	2.24	2.29	His284 Nε2	2.6
His504 Nε2	2.35	2.29	His289 Nε2	2.2
His690 Nε2	2.27	2.22	His469 Nε2	2.1
Asn694 Oδ1	2.85	2.27	Asn473 Oδ1	2.9
Ile839 O(C-term)	2.24	2.19	Val605 O(C-term)	2.4
Water O	2.11	2.23	Water O	2.3

[a]From PDB: 3PZW [14]; uncertainty: ± 0.004 Å. [b]From PDB: 4WFO; uncertainty: ± 0.003 Å. Distance uncertainties were determined from the overall maximum-likelihood coordinate error of the structure and are scaled for the B-factors of those atoms.[15] [c]From recent report of native Mn-containing lipoxygenase (2.0 Å; PDB: 5FNO) from Fungus, *Magnaporthe oryzae.*[16]

Table S3. The bond and angle parameters associated with the Mn-ligand interactions for the MD simulations.

	equilibrium distance (Å)	force constant ((kcal/mol) Å^{-2})
Mn-Owater	2.28	237.3
Mn-O839	2.11	237.3
Mn-O694	2.23	237.3
Mn-N499	2.24	135.8
Mn-N504	2.34	135.8
Mn-N690	2.31	135.8

	equilibrium angle (°)	force constant ((kcal/mol) Å^{-2})
X-Mn-Y[a]	90 or 180[b]	125
Mn-O-H	126.8	100

[a] X and Y are the ligand atoms bound to Mn.
[b] The Mn center and ligands form an octahedral structure, so these angles are either 90 or 180 degrees.

Table S4. Average C11−O Distances Obtained from Equilibrium Molecular Dynamics Trajectories with ENDOR-Derived C11−Mn and C10−Mn Distances as Restraints[a]

	"Carboxylate in" model		"Carboxylate out" model	
	R_{eq} (C11−O), Å	γ (C11-Mn-O), °	R_{eq} (C11−O), Å	γ (C11-Mn-O), °
WT	3.1 ± 0.1	25 ± 4	4.2 ± 0.2	58 ± 5
I553G	3.9 ± 0.2	31 ± 8	5.1 ± 0.2	64 ± 5
DM	4.1 ± 0.2	29 ± 7	4.9 ± 0.2	56 ± 5

[a]On the basis of the ENDOR analysis, two harmonic restraints were applied such that the equilibrium C11−Mn distance was set to 4.9, 5.6, and 5.8 Å for the WT, I553G, and DM species, respectively, and the equilibrium C10−Mn distance was set to 4.8 Å for all three species, with a force constant of 200 kcal/mol A^{-2}. The reported C11−O distances (R_{eq}) and C11-Mn-O angles (γ) are averaged over two independent 50 ns trajectories for each species. The reported error bars are standard deviations and do not reflect systematic errors due to limitations in the force field and conformational sampling.

References

(1)   Fender, B. E.; Figgis, B. N.; Forsyth, J. B.; Reynolds, P. A.; Stevens, E. *Proc. R. Soc. London* **1986**, *404*, 127-138.

(2)   Wenzel, T. J.; Bettes, T. C.; Sadlowski, J. E.; Sievers, R. E. *J. Am. Chem. Soc.* **1980**, *102*, 5904-5906.

(3)   Hoffman, B. M.; Martinsen, J.; Venters, R. A. *J. Magn. Reson.* **1984**, *59*, 110-123.

(4)   Hoffman, B. M.; Gurbiel, R. J.; Werst, M. M.; Sivaraja, M. In *Advanced EPR, Applications in Biology and Biochemistry*; Hoff, A. J., Ed.; Elsevier: Amsterdam, 1989, p 541-591.

(5)   DeRose, V. J.; Hoffman, B. M. In *Methods Enzymol.*; Sauer, K., Ed.; Academic Press: New York, 1995; Vol. 246, p 554-589.

(6)   Tan, X.; Bernardo, M.; Thomann, H.; Scholes, C. P. *J. Chem. Phys.* **1993**, *98*, 5147-5157.

(7)   McNaughton, R. L.; Reddi, A. R.; Clement, M.; Sharma, A.; Barnese, K.; Rosenfeld, L.; Gralla, E. B.; Valentine, J. S.; Culotta, V. C.; Hoffman, B. M. *Proc. Natl. Acad. Sci. U. S. A.* **2010**, *107*, 15335-15339.

(8)   Offenbacher, A. R.; Zhu, H.; Klinman, J. K. *Tetrahedron Lett.* **2016**, *57*, 4537-4540.

(9)   Knapp, M. J.; Rickert, K. W.; Klinman, J. K. *J. Am. Chem. Soc.* **2002**, *124*, 3865-3874.

(10)   Hu, S.; Sharma, S. C.; Scouras, A. D.; Soudackov, A. V.; Carr, C. A. M.; Hammes-Schiffer, S.; Alber, T.; Klinman, J. K. *J. Am. Chem. Soc.* **2014**, *136*, 8157-8160.

(11)   Meyer, M. P.; Tomchick, D. R.; Klinman, J. K. *Proc. Natl. Acad. Sci. U. S. A.* **2008**, *105*, 1146-1151.

(12)   Su, C.; Oliw, E. H. *J. Biol. Chem.* **1998**, *273*, 13072-13079.

(13)   Su, C.; Sahlin, M.; Oliw, E. H. *J. Biol. Chem.* **2000**, *275*, 18830-18835.

(14)   Minor, W.; Steczko, J.; Stec, B.; Otwinowski, Z.; Bolin, J. T.; Walter, R.; Axelrod, B. *Biochemistry* **1996**, *35*, 10687-10701.

(15)   Murshudov, G. N.; Vagin, A.; Dodson, E. J. *Acta Cryst.* **1997**, *D53*, 240-255.

(16)   Wennman, A.; Oliw, E. H.; Karkehabadi, S.; Chen, Y. *J. Biol. Chem.* **2016**, *291*, 8130-8139.